www.sciencemag.org/cgi/content/full/science.1224030/DC1

Supplementary Material for

Earthquake in a Maze: Compressional Rupture Branching During the 2012 M_w 8.6 Sumatra Earthquake

L. Meng,* J.-P. Ampuero, J. Stock, Z. Duputel, Y. Luo, V. C. Tsai

*To whom correspondence should be addressed. E-mail: lsmeng@gps.caltech.edu

Published 19 July 2012 on *Science* Express
DOI: 10.1126/science.1224030

This PDF file includes:

Other Supplementary Material for this manuscript includes the following:
(available at www.sciencemag.org/cgi/content/full/science.1224030/DC1)

Movies S1 and S2

Materials and Methods

Back-projection data selection and processing:

We processed the seismic data recorded by various seismic arrays at epicentral distances between 30 and 90 degrees. The large aperture and dense spacing of the European (www.orfeus-eu.org; Figure S1) and Japanese Hi-net networks (www.hinet.bosai.go.jp; Figure S2) provided fine spatial resolution for this event. The two arrays are located at almost orthogonal azimuths relative to the source area, providing complementary views of the rupture process. The P waveforms were filtered between 0.5 and 1 Hz, selected by their signal-to-noise ratio and by the mutual coherency of their initial 10 seconds, and then aligned by multi-channel cross-correlation. We applied the MUSIC back-projection technique (*4*, *31*) on sliding windows ten seconds in length. This source imaging technique allows tracking the migration of the multiple sources of high-frequency (HF) radiation of an earthquake rupture. Our particular approach combines a high-resolution array processing technique (*32*, *33*) with multi-taper cross-spectral estimation (*34*) to achieve higher resolution than conventional beamforming. Adopting a "reference window" strategy avoids the systematic "swimming" artifact (*5*). The MUSIC pseudo-spectrum is back-projected into the off-Sumatra region based on P travel times computed by the Tau-P toolkit and the IASP91 model (*36*)

Multiple point source analysis:

Seismic waves from the 2012 Sumatra earthquake sequence were recorded by a large number of broadband seismic stations enabling robust and reliable characterization of the overall source characteristics at long periods. For the Mw=8.6 event, 113 channels were used to perform a multiple point source inversion. We inverted simultaneously for the moment tensors of the subevents, their locations (latitude, longitude, depth) and time delays using a global sampling approach. The inversion is performed using the W-phase waveforms at shorter period (150-500 s) than the usual practice for single point source inversions of Mw>8.0 earthquakes. The optimal centroid depth of the mainshock is 30 km. Our preferred model is a two point source solution which is presented on Fig. 1.

Resolution and uncertainty of back-projection source imaging:

We conducted several analyses to understand the strengths and limitations of our back-projection method, as specifically applied to the European and Japanese arrays. We address two different array performance criteria. The spatial *resolution* of an array is defined as the capability to separate two simultaneous sources of different location: the *resolution length* is the minimum distance between sources that can be distinguished without ambiguity. The spatial *uncertainty* of an array is defined as the error in estimates of source location for isolated sources.

The resolution length that can be achieved with linear beamforming is conventionally estimated as the width at half peak amplitude of the main lobe of the array response function (ARF, *35*). Figs. S4 and S5 show the ARFs of the Japanese and the European networks back-projected into the off-Sumatra region. The European ARF is relatively

compact with resolution lengths of 35 km in the N-S direction and 65 km in the E-W direction. These are one order of magnitude smaller than the source dimension of the M8.6 off-Sumatra event, which indicates that the overall rupture process can be resolved as long as there is adequate signal coherence. The Japanese Hi-Net array has a larger and more anisotropic ARF, with resolution lengths of 450 km in the N-S direction and 70 km in the E-W direction. This helps explaining why the early separation of the bilateral rupture fronts on fault B is imaged by the European array (movie S2) but the two fronts appear simultaneously in the Hi-Net images only when they reach the ends of fault B.

In back-projection source imaging with linear beamforming, the estimation of source location is based on identifying the peak position of an image that is smeared by the array response. The Cramer-Rao bound, a theoretical estimate of the upper bound of uncertainty of an estimator, indicates that the source location uncertainty is proportional to the resolution length of the ARF and inversely proportional to the signal-to-noise ratio of the images (SNR), defined as the ratio between the main peak amplitude and the mean amplitude of the background peaks of the image. The SNR depends on both the signal quality (noise and multipath) and the station density (sidelobe amplitude). The Hi-Net array has a particularly large SNR due to its small ambient noise level (borehole stations) and extremely dense spacing (~20 km).

However, due to the nonlinearity of the MUSIC technique, its resolution cannot be fully appreciated by considering the ARF. Typically, the resolution length of MUSIC is at least two times smaller than the beamforming resolution length (*31*). Moreover, the resolution analysis based on the ARF assumes perfect signal coherence. In practice, we quantify the uncertainty of back-projection of Hi-Net data by bootstrapping the back-projection of a M6.1 aftershock that occurred on April 21th, 2012 at 93.39 degree E and 2.22 degree N. The aftershock seismograms are first aligned by the initial 3 s of the P-wave arrival. The noise at each station is computed as the waveform residual with respect to the array-stacked waveform. The noise is shuffled by randomizing its Fourier phase spectrum, then added back to the stack. One thousand synthetic realizations of the aftershock array recordings plus noise are then back-projected considering the 10-s long window that begins at the initial arrival. The resulting back-projection locations are shown in Fig. S6. The bootstrap 95% confidence ellipse is elongated along the N-S direction with a major axis length of 9.5 km and minor axis length of 2.8 km. Unfortunately, the recording of this aftershock at the European array is too weak to be used in the 0.5-1 Hz frequency band.

To further understand the performance of the back-projection on complicated ruptures, we conduct two synthetic earthquake scenarios. To include key characteristics of the real wavefield, such as the decay of waveform coherence as a function of time, we use the M6.1 event as empirical Green's function. Inspired by our final back-projection result, particularly a jump from the fault C to fault D imaged with the Hi-Net array, we test scenarios of bilateral rupture on Fault A and B and unilateral rupture on Fault C with (Fig.S7) or without (Fig.S8) an additional fault D. We consider a uniform distribution of sub-sources, regularly located every 15 km along each fault. The rupture times correspond to an assumed rupture speed of 2.5 km/s. The MUSIC back-projection

technique recovers the location and timing of the scenario sources very well. The uncertainty of the peak locations is less than 20 km, which is reasonably good considering the coda and interference between sub-sources. These synthetic tests indicate that the jump between faults C and D is resolvable by the Hi-Net array.

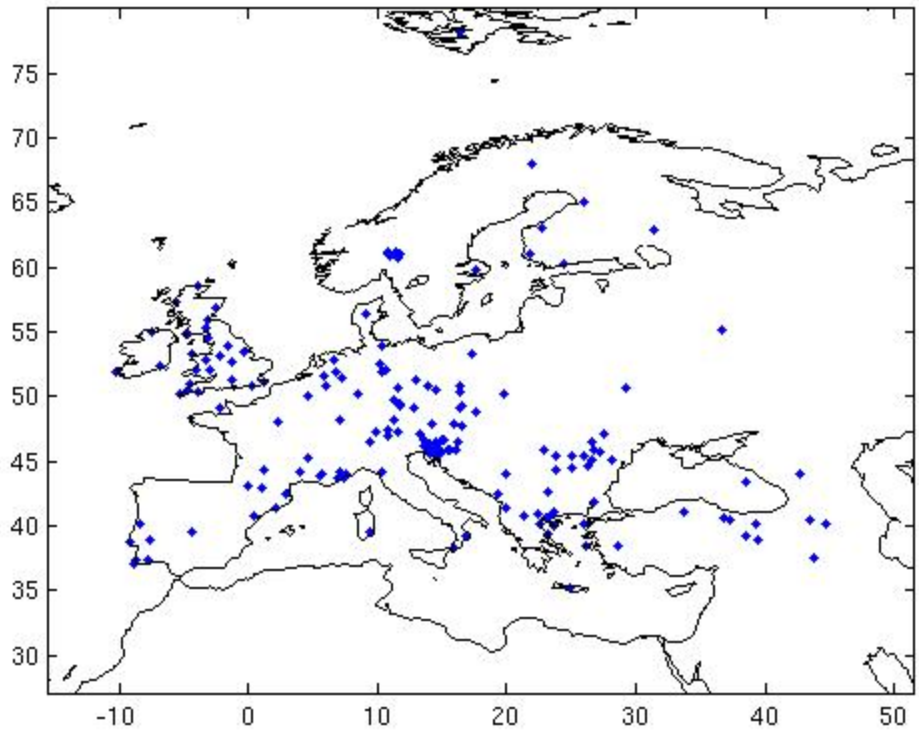

Fig. S1
Selected stations used for back-projection from the European network.

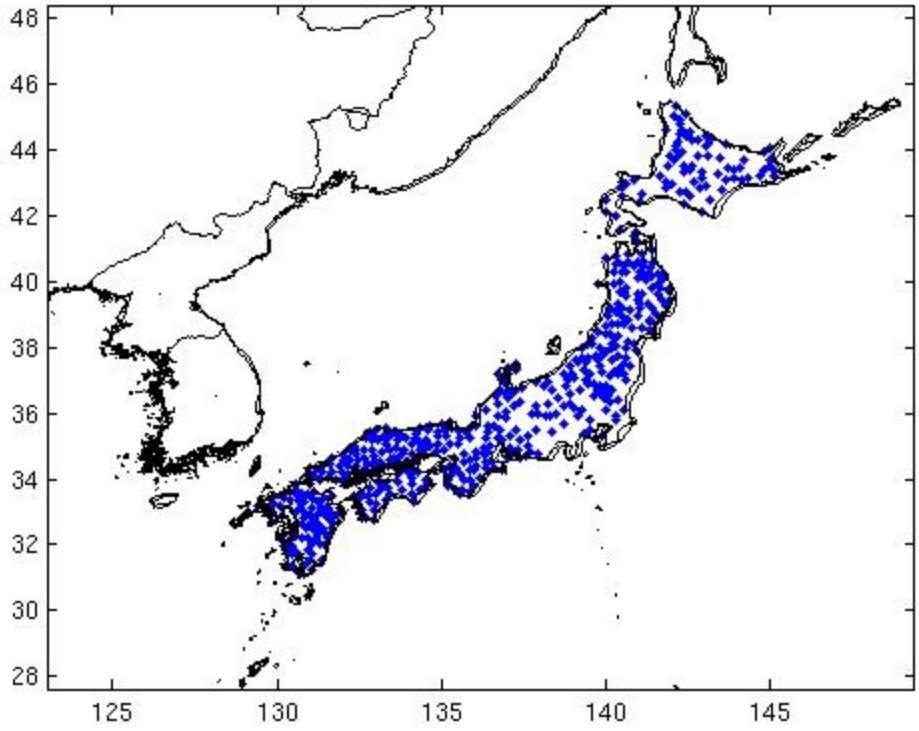

Fig. S2
Selected stations for back-projection from the Hi-Net (Japan) network.

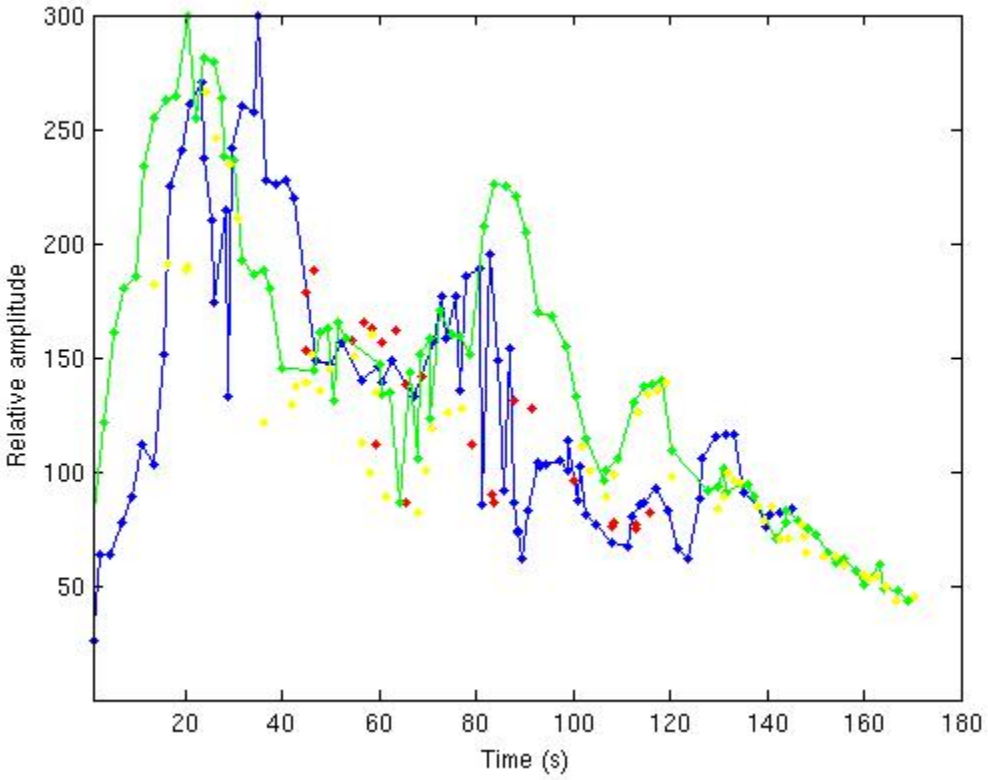

Fig. S3

Beamforming source amplitude evaluated at the location of the HF radiators obtained by MUSIC as a function of time, obtained with the European array (green) and Japanese Hi-Net array (blue). The scale is normalized by the beamforming amplitude of the initial window. The yellow and red dots indicate the amplitude of the secondary sources for the European and Japanese arrays, respectively.

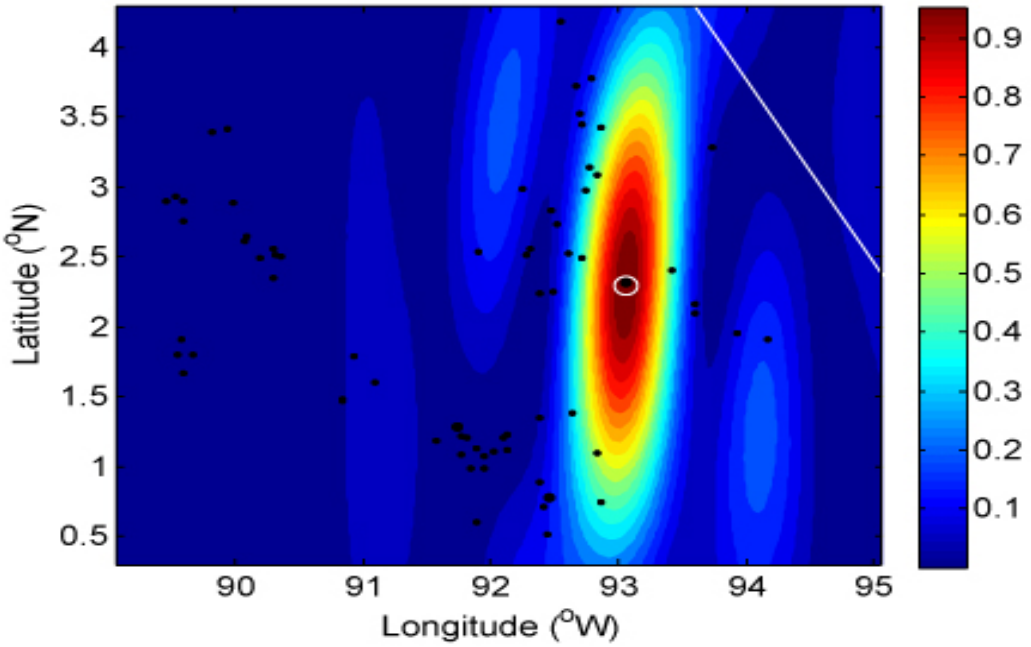

Fig. S4

Array response pattern of the Japanese Hi-Net array back-projected into the off-Sumatra earthquake region, plotted in map view. The color scale indicates the power of the array response, normalized by its peak value. The white line denotes the trace of the Sumatra trench. The white circle is the location of the epicenter. The black dots are early aftershocks that occurred within 24 hours of the mainshock.

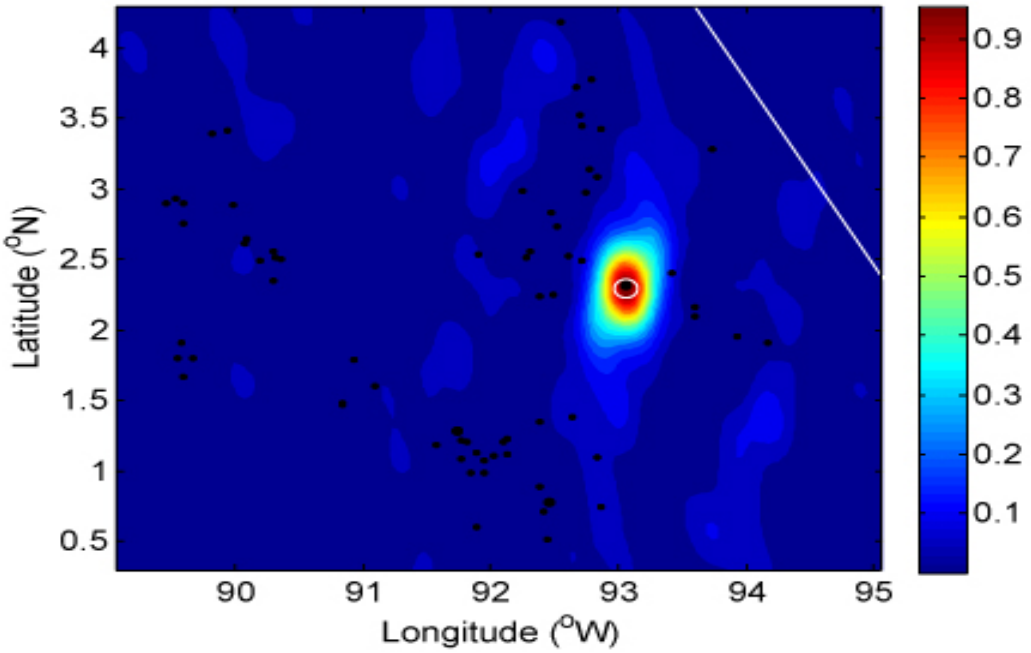

Fig. S5

Array response pattern of the European network. The convention is the same as in the previous figure.

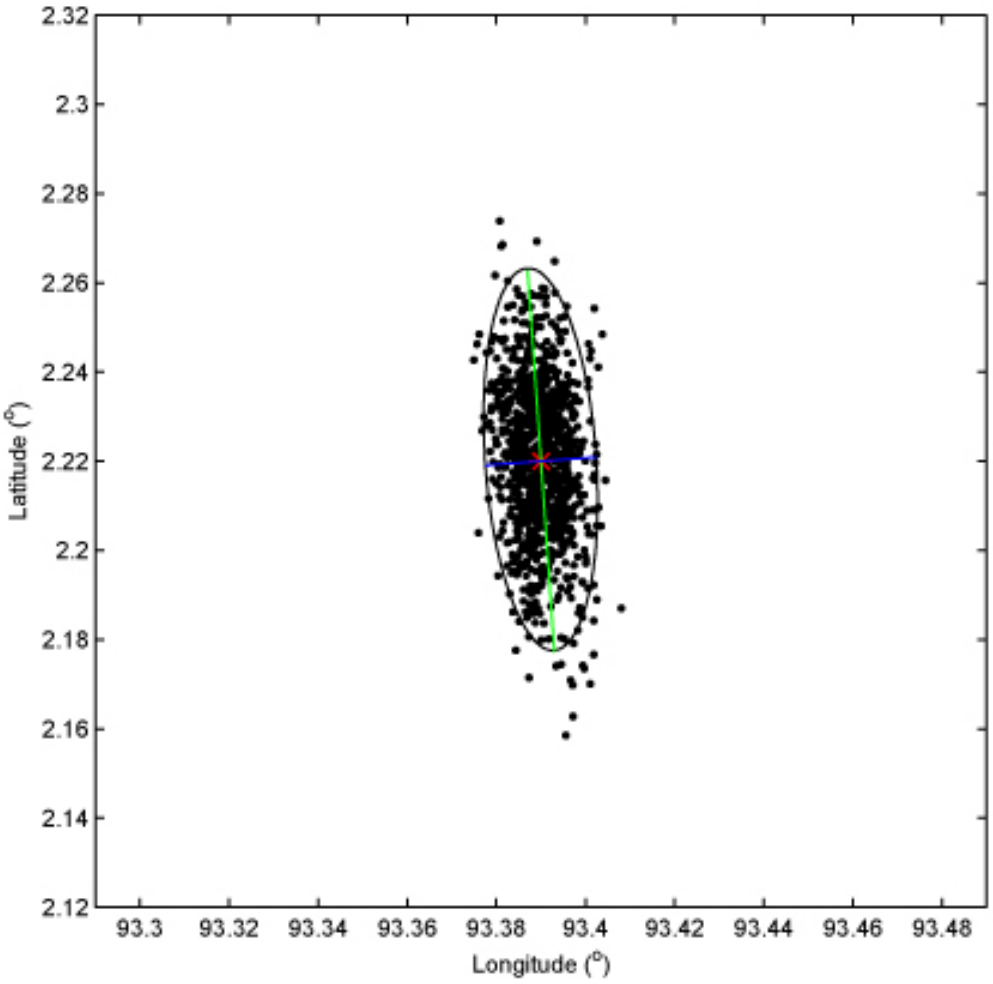

Fig. S6

Uncertainty of the back-projection. A M6.1 aftershock that occurred on April 21th, 2012 is used here as an empirical Green's function. The red asterisk denotes the hypocenter. The black dots are the back-projection of the bootstrapped aftershock recordings. The ellipse is the 95% confidence interval. It has a 9.5 km long major axis (blue line) and 2.8 km long minor axis (green line).

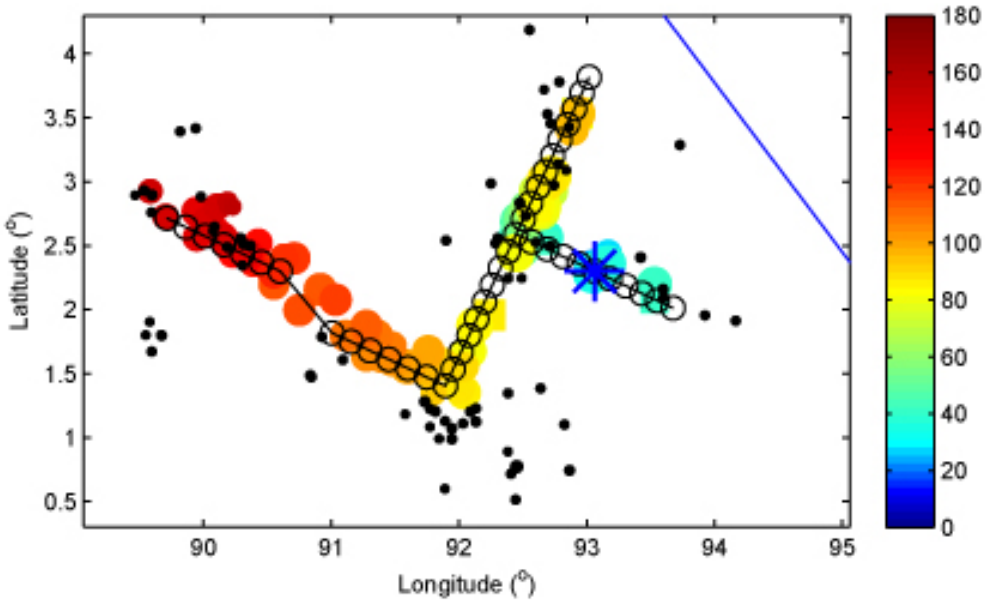

Fig. S7

Back-projection of a synthetic rupture scenario. The black circles are the synthetic sources. The colored circles are the recovered back-projection locations color-coded by time. The black dots are the early aftershocks that occurred within 24 hours of the mainshock.

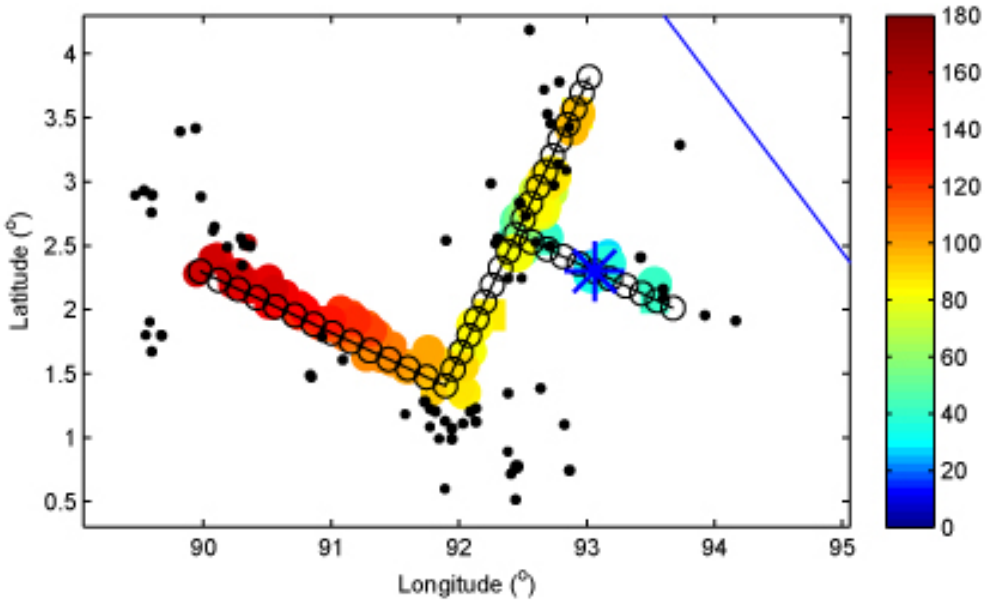

Fig. S8

Back-projection of a synthetic rupture scenario without offset between faults C and D. The convention of the figure is the same as in the previous one.

Movie S1

The movie shows the raw results of back-projection source imaging based on teleseismic data from European networks. Warm colors indicate the positions of the high frequency (0.5 to 1 Hz) radiation back-projected onto the source region based on IASP91 travel times (*36*). The sliding window is 10-s long and the origin time is 08:38:37, 04-12-12 (UTC). The beginning of the sliding window is set to be 5 s before the initial P-wave arrival. Colors indicate the amplitude of the MUSIC pseudo-spectrum on a logarithmic scale (dB) after subtracting the background level and rescaling the maximum to the linear beamforming power in each frame separately. The white star is the mainshock epicenter and the green circles are the epicenters of the first day of aftershocks from the NEIC catalog. Time relative to hypocentral arrival time is shown on top. The trench and coastlines are shown by white curves.

Movie S2

Back-projection source imaging based on teleseismic data from Japanese networks. Same convention as the previous movie.

References and Notes

1. E. R. Engdahl, A. Villasenor, H. R. DeShon, C. H. Thurber, Teleseismic relocation and assessment of seismicity (1918-2005) in the region of the 2004 Mw 9.0 Sumatra-Andaman and 2005 Mw 8.6 Nias Island great earthquakes. *Bull. Seismol. Soc. Am.* **97**, (1A), S43 (2007). doi:10.1785/0120050614

2. G. L. Choy, A. McGarr, Strike-slip earthquakes in the oceanic lithosphere: observations of exceptionally high apparent stress. *Geophys. J. Int.* **150**, 506 (2002). doi:10.1046/j.1365-246X.2002.01720.x

3. S. Cloetingh, R. Wortel, Stress in the Indo-Australian Plate. *Tectonophysics* **132**, 49 (1986). doi:10.1016/0040-1951(86)90024-7

4. L. Meng, A. Inbal, J. P. Ampuero, A window into the complexity of the dynamic rupture of the 2011 Mw 9 Tohoku-Oki earthquake. *Geophys. Res. Lett.* **38**, L00G07 (2011). doi:10.1029/2011GL048118

5. L. Meng, J. P. Ampuero, Y. Luo, W. Wu, S. Ni, Mitigating Artifacts in Back-Projection Source Imaging with Implications on Frequency-Dependent Properties of the Tohoku-Oki Earthquake. *Earth Planets Space* 10.5047/eps.2012.05.010 (2012).

6. D. L. Wells, K. J. Coppersmith, New Empirical Relationships among Magnitude, Rupture Length, Rupture Width, Rupture Area, and Surface Displacement. *Bull. Seismol. Soc. Am.* **84**, 974 (1994).

7. D. A. Wiens, S. Stein, Age Dependence of Oceanic Intraplate Seismicity and Implications for Lithospheric Evolution. *J. Geophys. Res.* **88**, (B8), 6455 (1983). doi:10.1029/JB088iB08p06455

8. M. Delescluse, N. Chamot-Rooke, Serpentinization pulse in the actively deforming Central Indian Basin. *Earth Planet. Sci. Lett.* **276**, 140 (2008). doi:10.1016/j.epsl.2008.09.017

9. D. P. Robinson, C. Henry, S. Das, J. H. Woodhouse, Simultaneous rupture along two conjugate planes of the Wharton Basin earthquake. *Science* **292**, 1145 (2001). doi:10.1126/science.1059395 Medline

10. M. Antolik, A. Kaverina, D. S. Dreger, Compound rupture of the great 1998 Antarctic plate earthquake. *J. Geophys. Res. Solid Earth* **105**, (B10), 23825 (2000). doi:10.1029/2000JB900246

11. B. P. Allmann, P. M. Shearer, Global variations of stress drop for moderate to large earthquakes. *J. Geophys. Res.* **114**, (B1), B01310 (2009). doi:10.1029/2008JB005821

12. A. Oth, D. Bindi, S. Parolai, D. Di Giacomo, Earthquake scaling characteristics and the scale-(in)dependence of seismic energy-to-moment ratio: Insights from KiK-net data in Japan. *Geophys. Res. Lett.* **37**, L19304 (2010). doi:10.1029/2010GL044572

13. J. C. Rollins, R. S. Stein, Coulomb stress interactions among M >= 5.9 earthquakes in the Gorda deformation zone and on the Mendocino Fault Zone, Cascadia subduction zone, and northern San Andreas Fault. *J. Geophys. Res.* **115**, (B12), B12306 (2010). doi:10.1029/2009JB007117

14. W. W. Sager *et al*., Large fault fabric of the Ninetyeast Ridge implies near-spreading ridge formation. *Geophys. Res. Lett.* **37**, L17304 (2010). doi:10.1029/2010GL044347

15. M. Delescluse, N. Chamotrooke, Instantaneous deformation and kinematics of the India-Australia Plate. *Geophys. J. Int.* **168**, 818 (2007). doi:10.1111/j.1365-246X.2006.03181.x

16. C. Deplus *et al*., Direct evidence of active deformation in the eastern Indian oceanic plate. *Geology* **26**, 131 (1998). doi:10.1130/0091-7613(1998)026<0131:DEOADI>2.3.CO;2

17. H. Horikawa, Earthquake doublet in Kagoshima, Japan: Rupture of asperities in a stress shadow. *Bull. Seismol. Soc. Am.* **91**, 112 (2001). doi:10.1785/0119990131

18. R. E. Abercrombie, M. Antolik, G. Ekstrom, The June 2000 M-w 7.9 earthquakes south of Sumatra: Deformation in the India-Australia Plate. *J. Geophys. Res.* **108**, (B1), 2018 (2003). doi:10.1029/2001JB000674

19. F. Klingelhoefer *et al*., Limits of the seismogenic zone in the epicentral region of the 26 December 2004 great Sumatra-Andaman earthquake: Results from seismic refraction and wide-angle reflection surveys and thermal modeling. *J. Geophys. Res.* **115**, (B1), B01304 (2010). doi:10.1029/2009JB006569

20. M. Cocco, J. R. Rice, Pore pressure and poroelasticity effects in Coulomb stress analysis of earthquake interactions. *J. Geophys. Res.* **107**, (B2), 2030 (2002). doi:10.1029/2000JB000138

21. P. B. Kelemen, G. Hirth, A periodic shear-heating mechanism for intermediate-depth earthquakes in the mantle. *Nature* **446**, 787 (2007). doi:10.1038/nature05717 Medline

22. J. J. McGuire, G. C. Beroza, Geophysics. A rogue earthquake off Sumatra. *Science* **336**, 1118 (2012). doi:10.1126/science.1223983 Medline

23. J. Escartín, G. Hirth, B. Evans, Strength of slightly serpentinized peridotites: Implications for the tectonics of oceanic lithosphere. *Geology* **29**, 1023 (2001). doi:10.1130/0091-7613(2001)029<1023:SOSSPI>2.0.CO;2

24. H. Jung, H. W. Green, II, L. F. Dobrzhinetskaya, Intermediate-depth earthquake faulting by dehydration embrittlement with negative volume change. *Nature* **428**, 545 (2004). doi:10.1038/nature02412 Medline

25. S. G. Wesnousky, Predicting the endpoints of earthquake ruptures. *Nature* **444**, 358 (2006). doi:10.1038/nature05275 Medline

26. T. Lay, C. J. Ammon, H. Kanamori, M. J. Kim, L. Xue, Outer trench-slope faulting and the 2011 M(w) 9.0 off the Pacific coast of Tohoku Earthquake. *Earth Planets Space* **63**, 713 (2011). doi:10.5047/eps.2011.05.006

27. Y. Tanioka, K. Satake, Tsunami generation by horizontal displacement of ocean bottom. *Geophys. Res. Lett.* **23**, 861 (1996). doi:10.1029/96GL00736

28. M. Chlieh *et al*., Coseismic slip and afterslip of the great M-w 9.15 Sumatra-Andaman earthquake of 2004. *Bull. Seismol. Soc. Am.* **97**, (1A), S152 (2007). doi:10.1785/0120050631

29. C. DeMets, R. G. Gordon, D. F. Argus, Geologically current plate motions. *Geophys. J. Int.* **181**, 1 (2010). doi:10.1111/j.1365-246X.2009.04491.x

30. A. N. B. Poliakov, R. Dmowska, J. R. Rice, Dynamic shear rupture interactions with fault bends and off-axis secondary faulting. *J. Geophys. Res.* **107**, (B11), 2295 (2002). doi:10.1029/2001JB000572

31. L. Meng, J. P. Ampuero, A. Sladen, H. Rendon, High-resolution backprojection at regional distance: Application to the Haiti M7.0 earthquake and comparisons with finite source studies. *J. Geophys. Res.* **117**, (B4), B04313 (2012). doi:10.1029/2011JB008702

32. R. O. Schmidt, Multiple Emitter Location and Signal Parameter-Estimation. *IEEE Trans. Antenn. Propag.* **34**, 276 (1986). doi:10.1109/TAP.1986.1143830

33. P. Goldstein, R. J. Archuleta, Deterministic Frequency-Wave-Number Methods and Direct Measurements of Rupture Propagation during Earthquakes Using a Dense Array - Data-Analysis. *J. Geophys. Res.* **96**, (B4), 6187 (1991). doi:10.1029/90JB02472

34. D. J. Thomson, Spectrum Estimation and Harmonic-Analysis. *Proc. IEEE* **70**, 1055 (1982). doi:10.1109/PROC.1982.12433

35. S. Rost, C. Thomas, Array seismology: Methods and applications. *Rev. Geophys.* **40**, 1008 (2002). doi:10.1029/2000RG000100

36. J. A. Snoke, Traveltime Tables for IASP91 and AK135. *Seismol. Res. Lett.* **80**, 260 (2009). doi:10.1785/gssrl.80.2.260